nature communications

Article

https://doi.org/10.1038/s41467-026-69748-8

Synergistic sulfur-chlorine battery chemistry towards efficient energy storage

Received: 5 December 2024

Accepted: 9 February 2026

Published online: 23 February 2026

Check for updates

Xiaoju Zhao[1,4], Meng Liao[2,3,4], Shitao Geng[1,4], Yan Wang[1], Shuo Wang[1], Zhaofeng Ouyang[1], Qiuchen Xu[1], Bin Yuan[1], Chengxiao Zhang[1], Shanshan Tang[1], Lei Ye[2], Liang Wu[1], Huisheng Peng[2] ✉ & Hao Sun[1] ✉

Conversion-type batteries with high energy storage efficiencies are crucial to minimize the energy loss during energy storage. However, current conversion-type batteries generally show relatively low energy storage efficiencies of (59–95)% with large charge-discharge overpotentials of 200–1500 mV. Here we report a rechargeable battery with a maximum energy storage efficiency of 99.5% and a small overpotential of 9 mV, based on a S-Cl synergistic chemistry with fast reaction kinetics. We verify that the in situ formed Cl_2 during charging can trigger highly efficient SO_2/SO_2Cl_2 conversion with a maximum current density of 400 mA/cm^2, which is one to three orders of magnitude higher than those of state-of-the-art conversion-type batteries. In addition, the high energy storage efficiencies of (93 – 97)% have been validated under a variety of harsh yet practical conditions, *e.g.*, at a low temperature of – 20 °C and a high areal capacity of 13.5 mAh/cm^2. We further demonstrate their potential applications by producing a 250 mAh pouch cell, an on-chip microbattery, and a wearable fiber battery, which exhibit high electrochemical properties and practicability.

Energy and environmental sustainability are critical challenges facing modern society, which demands transformative energy storage technologies to maximize the utilization of renewable electricity[1–3]. However, the energy storage efficiency—defined as the ratio of energy output to input—has stagnated for current energy storage technologies such as pumped hydro energy storage, due to the severe energy loss during the energy conversion among electricity-kinetic energy-gravitational potential energy[4]. Estimated with an average energy storage efficiency of ~75%, the energy loss of the global renewable energy storage might exceed 3000 terawatt-hour (TWh) in 2023[5], thus demanding energy storage technologies with both high energy density and energy storage efficiency to promote the utilization of renewable electricity[6,7].

Electrochemical energy storage offers a promising solution to these challenges. Among various options, conversion-type batteries show promise for grid-scale renewable energy storage due to their high material abundance, cost-effectiveness, and energy density[8,9]. However, the energy storage efficiencies of common conversion-type batteries are typically in the range of 59% to 95%, with large charge–discharge overpotentials of 200 to 1500 mV (Supplementary Table 1)[10–13]. This can be attributed to the slow kinetics of the redox chemistries, involving significant energy barriers for the redox processes in these conversion-type batteries[14,15]. Therefore, it is important yet challenging to develop conversion-type batteries with fast reaction kinetics.

Results

We demonstrate that, by presenting synergistic S-Cl chemistry with fast kinetics at the positive electrode, high energy storage efficiencies can be realized in a rechargeable Li||SO_2Cl_2-Cl_2 battery. The battery comprises a ketjenblack carbon positive electrode, a Li metal negative

[1]Frontiers Science Center for Transformative Molecules, State Key Laboratory of Synergistic Chem-Bio Synthesis, School of Chemistry and Chemical Engineering, and Zhangjiang Institute for Advanced Study, Shanghai Jiao Tong University, Shanghai, China. [2]State Key Laboratory of Molecular Engineering of Polymers, Department of Macromolecular Science, and Institute of Fiber Materials and Devices, Fudan University, Shanghai, China. [3]Department of Mechanical Engineering, The Pennsylvania State University, University Park, PA, USA. [4]These authors contributed equally: Xiaoju Zhao, Meng Liao, Shitao Geng. ✉e-mail: penghs@fudan.edu.cn; haosun@sjtu.edu.cn

electrode, and a non-flammable electrolyte based on the mixture of 3.6 M LiCl and 3.6 M $AlCl_3$ dissolved in sulfuryl chloride (SO_2Cl_2), referred to as the LAS electrolyte (Fig. 1a). In this electrolyte, SO_2Cl_2 serves as both the solvent and catholyte, and $AlCl_3$ facilitates the dissolution of LiCl salt with the formation of $AlCl_4^-$ anions and Li^+ ions (Supplementary Fig. 1a). During initial discharge, the battery reaction involves SO_2Cl_2 reduction with the formation of SO_2 and LiCl on the positive electrode, and the stripping of Li metal on the negative electrode as described in Eq. 1 (Supplementary Fig. 1a-d). An initial discharge voltage of ~3.87 V (Supplementary Fig. 1b) was consistent with the discharge plateau for the SO_2Cl_2/SO_2 reduction reaction in Li||SO_2Cl_2 primary battery[16–19]. The lower plateau of ~3.18 V in rechargeable Cl_2 battery may be attributed to the different solvation properties derived from the $SOCl_2$-based electrolyte, as well as the parasitic reactions involving Cl_2 (primary charge product), SO_2 (initial discharge product), and $SOCl_2$ (electrolyte solvent and catholyte).

$$2Li + SO_2Cl_2 \rightarrow 2LiCl + SO_2 \quad (1)$$

The positive electrode reduction pathway can be controlled by the electrochemical protocol. When operated with a capacity-limited protocol at a specific capacity of up to ~4000 mAh/g based on the mass of carbon unless otherwise specified, the battery exhibited a high discharge voltage of ~3.9 V with a high energy storage efficiency of ~99.5% (Fig. 1b). The positive electrode reaction involves a reversible redox chemistry based on SO_2/SO_2Cl_2 and $LiCl/Cl_2$ redox couples (Eq. 2), as verified by the reversible variations of ion intensities of SO_2^+ ($m/z = 64$) and Cl_2^+ ($m/z = 70$) during charge and discharge measured by differential electrochemical mass spectrometry (DEMS) (Fig. 1c). Further validation came from S *K*-edge X-ray absorption (XAS) spectra, which indicated the re-generation of SO_2Cl_2 at the charged state through the detected fragment ions at 2478.3 eV and 2482.4 eV[20] (Fig. 1d). The formation of Cl_2 was also confirmed by the pre-edge peak at 2822.7 eV in Cl *K*-edge XAS spectra[21,22] (Fig. 1e). Upon discharge, the consumption of SO_2Cl_2 and Cl_2 was observed, along with the formation of SO_2 (2475.6 eV in Fig. 1d) and LiCl (2829.3 eV in Fig. 1e and Supplementary Fig. 2a-f)[20], which was consistent with the positive electrode reaction proposed in Eq. 2, as confirmed by in situ DEMS

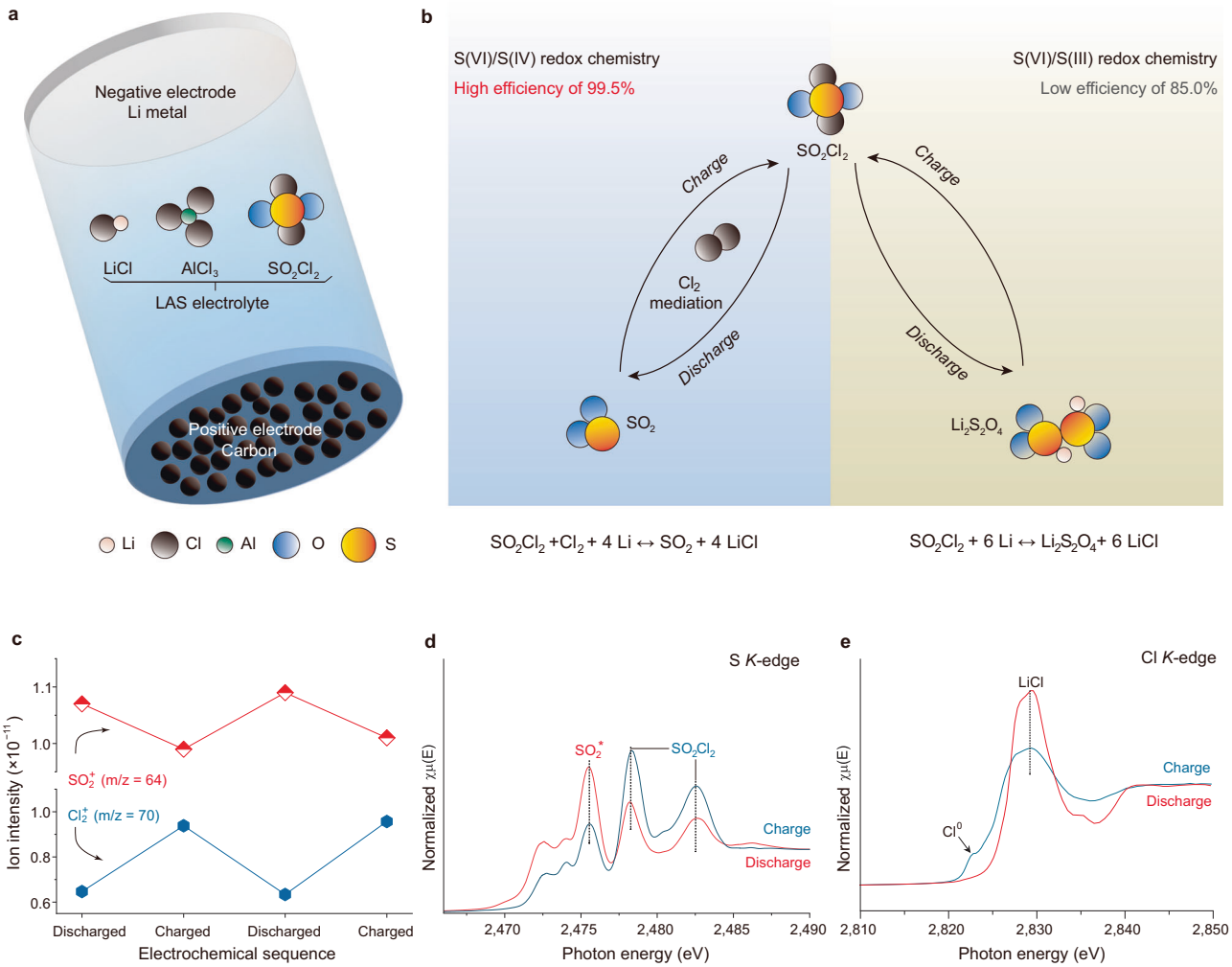

Fig. 1 | Rechargeable Li||SO_2Cl_2-Cl_2 battery with a high energy storage efficiency. a Schematic illustration of the rechargeable Li||SO_2Cl_2-Cl_2 battery composed of a Ketjenblack carbon positive electrode, a Li metal negative electrode, and a LiCl-$AlCl_3$-SO_2Cl_2 (LAS) electrolyte. **b** Comparison of the S(VI)/S(IV) and S(VI)/S(III) redox chemistries with and without Cl_2 mediation, respectively. **c** Variation of the ion intensities of SO_2^+ ($m/z = 64$) and Cl_2^+ ($m/z = 70$) acquired by DEMS for the rechargeable Li||SO_2Cl_2-Cl_2 battery at different charge and discharge states following the S(VI)/S(IV) redox chemistry. **d**, **e** S *K*-edge and Cl *K*-edge XAS profiles of the positive electrodes in rechargeable Li||SO_2Cl_2-Cl_2 batteries following the S(VI)/S(IV) pathway at the charge and discharge states, respectively. The XAS profiles were processed using the Athena software through pre-edge background subtraction and edge jump normalization. Source data for Fig. 1 are provided as a Source Data file.

https://doi.org/10.1038/s41467-026-69748-8

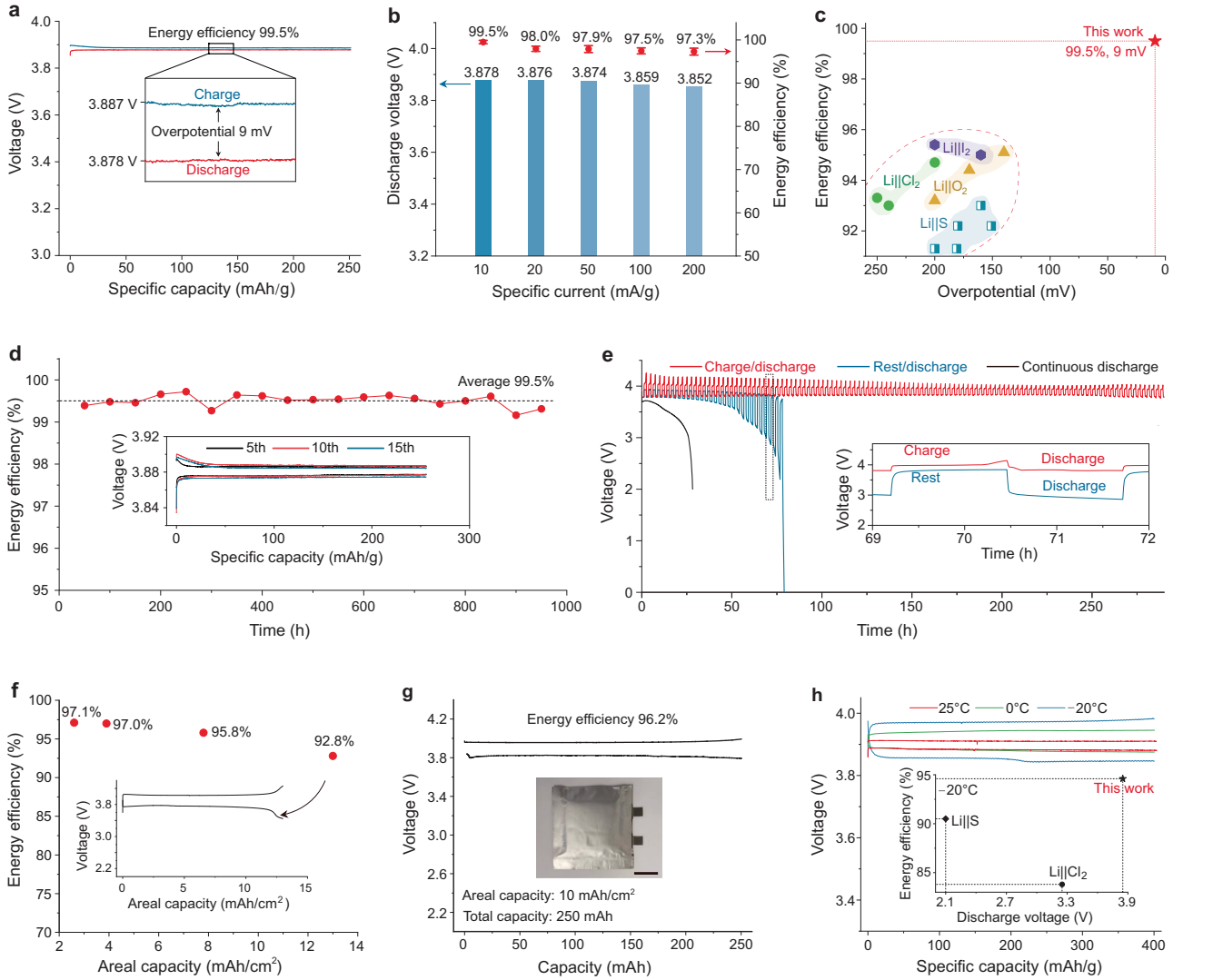

Fig. 2 | Electrochemical performance of rechargeable Li||SO_2Cl_2-Cl_2 battery. **a** Representative galvanostatic charge–discharge curve of the rechargeable Li||SO_2Cl_2-Cl_2 battery at a specific current of 10 mA/g. The inset shows the magnified charge–discharge curves with an overpotential of only 9 mV. **b** Variation of the average discharge voltage and energy storage efficiency at increasing specific currents from 10 to 200 mA/g. The energy storage efficiencies are presented as mean ± standard deviation. **c** Comparison of the energy storage efficiency and overpotential of the rechargeable Li||SO_2Cl_2-Cl_2 battery with state-of-the-art conversion-type Li metal batteries. More details are provided in Supplementary Table 1. **d** Cycling performance of the rechargeable Li||SO_2Cl_2-Cl_2 battery during 950 h at 10 mA/g, achieving an average energy storage efficiency of 99.5%. The inset shows the representative charge-discharge curves at the 5th, 10th, and 15th cycles. **e** Cycling performance of the rechargeable Li||SO_2Cl_2-Cl_2 batteries based on charge/discharge, rest/discharge, and continuous discharge protocols. The battery at rest condition was held at open-circuit voltage. The specific current is 400 mA/g. **f** Variation of discharge voltage and energy storage efficiency on different areal capacities from 2.6 to 13.5 mAh/cm^2 at a current density of 2.6 mA/cm^2 (400 mA/g). **g** Representative galvanostatic charge–discharge curves of a 250 mAh pouch cell with an areal capacity of 10 mAh/cm^2 at 0.25 mA/cm^2. The inset shows the 250 mAh pouch cell with a scale bar of 2 cm. **h** Representative galvanostatic charge–discharge curves and energy storage efficiencies of the rechargeable Li||SO_2Cl_2-Cl_2 batteries at different temperatures. The inset compares the energy storage efficiency and discharge voltage of the rechargeable Li||SO_2Cl_2-Cl_2 battery with state-of-the-art rechargeable Li||S[20–22] and Li||Cl_2[23,24] batteries at −20 °C. The specific charge–discharge capacity is 250 mAh/g in (**a**) and (**d**), and 500 mAh/g in (**b**) and (**e**). The areal capacities and current densities were based on the geometric area of the positive electrodes. The areas of the positive electrodes were 1.54 cm^2 in (**f**) and 16 cm^2 in (**g**). Source data for Fig. 2 are provided as a Source Data file.

(Supplementary Fig. 2g).

$$4LiCl + SO_2 - 4e^- \leftrightarrow SO_2Cl_2 + Cl_2 + 4Li^+ \quad (2)$$

For comparison, when the same battery was operated with a voltage-limited protocol at a cut-off discharge voltage of 2 V, it exhibited a much lower discharge voltage of ~3.5 V with an energy storage efficiency of only ~85%, following a different redox pathway based on reversible $SO_2Cl_2/Li_2S_2O_4$ conversion (Eq. 3).

$$2SO_2Cl_2 + 6Li^+ + 6e^- \leftrightarrow Li_2S_2O_4 + 4LiCl \quad (3)$$

By following the high-efficiency redox pathway, the battery exhibited a low charge–discharge overpotential of only 9 mV at 250 mAh/g and 10 mA/g, resulting in a high energy storage efficiency of 99.5% (Fig. 2a). High energy storage efficiencies of 99.5 – 97.3% were further validated at increasing specific currents from 10 to 200 mA/g, with a minimal decrease of only 26 mV for the discharge voltage, indicating the

fast reaction kinetics of the battery (Fig. 2b). These metrics are competitive compared to some recent relevant reports based on S, O_2, I_2, and Cl_2 positive electrodes (Fig. 2c). Moreover, the reversibility of the high energy storage efficiency was confirmed for over 950 h, achieving an average energy storage efficiency of 99.5% (Fig. 2d). To confirm the battery's rechargeability, we adopted a well-established method in rechargeable metal-air batteries[23], by testing another two identical batteries under a rest/discharge or continuous discharge protocol (Fig. 2e), which only delivered ~26% and ~20% of the total specific discharge capacity of the normally charged battery, respectively, confirming the rechargeability of the Li||SO_2Cl_2-Cl_2 battery.

We further validated the high energy storage efficiencies of these batteries under various conditions, for instance, a high areal capacity of 13.5 mAh/cm^2 which showed a decent energy storage efficiency of ~93% (Fig. 2f). In addition, a reversible energy storage efficiency of 95.8% was maintained over cycling at an areal capacity of 7.8 mAh/cm^2 (Supplementary Fig. 3a, b), with consistent Raman spectra of the cycled electrolyte, indicating the high stability of the LAS electrolyte (Supplementary Fig. 3c). For a 250 mAh pouch cell at an areal capacity of 10.0 mAh/cm^2, a high energy storage efficiency of 96.2% could be achieved (Fig. 2g), indicating the practicality of these high-efficiency batteries. In addition, we achieved the high energy storage efficiencies of 98.4% and 94.6% at 0 °C and −20 °C, respectively (Fig. 2h and Supplementary Fig. 3d), demonstrating competitive performance compared to Li||S[24–26] and Li||Cl_2[27,28] batteries at similarly low temperatures. The electrochemical stability of our Li||SO_2Cl_2-Cl_2 battery was confirmed by a decent shelf life of 60 days, which enabled potential applications in emergency backup power, deep-sea exploration, and space missions (Supplementary Fig. 3e).

To fully clarify the positive electrode chemistry, we investigated the charge and discharge products with different discharge voltages (Fig. 3a). With a high discharge voltage of ~3.9 V, XPS S 2*p* spectra confirmed the formation of SO_2 (S $2p_{3/2}$, 168.0 eV), in contrast to the formation of $Li_2S_2O_4$ (S $2p_{3/2}$, 166.8 eV) at ~3.5 V[29] (Fig. 3b), which agreed with the S(VI)/S(IV) and S(VI)/S(III) pathways described in Eqs. 2 and 3. The SO_2Cl_2 detected in both S(VI)/S(IV) and S(VI)/S(III) pathways is likely trapped within the nanopores of Ketjenblack carbon, even when thoroughly washed with solvent and treated under vacuum. Depth profiling of time-of-flight secondary ion mass spectroscopy (TOF-SIMS) further confirmed the formation of $Li_2S_2O_4$ during discharge, as verified by the ion fragments of $LiS_2O_3^-$, $LiSO_4^-$, and LiS_2O^- (Fig. 3c). Additionally, the S(VI)/S(IV) and S(VI)/S(III) pathways were validated by quantitative X-ray fluorescence (XRF) analysis, which demonstrated the correlation between the amount of LiCl formed on the discharged positive electrode and the discharge capacity (Fig. 3d), providing important insights to the redox chemistries of the positive electrode. DEMS exhibited the generation and consumption of SO_2Cl^+ signal ($m/z = 99$) during charge and discharge, respectively, indicating the involvement of SO_2Cl_2 as an active material in the S(VI)/S(III) pathway (Supplementary Fig. 4).

The origin of the high energy storage efficiency in our Li||SO_2Cl_2-Cl_2 battery draws our interest. In situ DEMS showed that signal intensities of Cl_2 measured in the battery following the S(VI)/S(IV) pathway were 6–10 times higher than those derived from the S(VI)/S(III) pathway (Fig. 3e, f). This suggested the crucial role of Cl_2 in mediating the S(VI)/S(IV) redox reaction, which reminded us of a well-known conversion reaction between SO_2, Cl_2, and SO_2Cl_2, with a small Gibbs free energy change of −1.09 eV and an equilibrium constant of 0.0288[16,30] (Eq. 4).

$$SO_2Cl_2 \rightarrow SO_2 + Cl_2 \quad (4)$$

Based on the voltage-limited protocol with a cut-off voltage of 2.0 V, we observed significant SO_2 formation after the initial discharge, as verified by the pronounced signals of SO_2^+ ($m/z = 64$) and SO^+ ($m/z = 48$) (Supplementary Fig. 5). According to Le Chatelier's principle, the substantial formation of SO_2 under a voltage-limited protocol can hinder Cl_2 formation during charging[31], as evidenced by the low Cl_2 levels detected by in situ DEMS (Fig. 3f). In contrast, the capacity-limited protocol avoids excessive SO_2 accumulation, thereby allowing the presence of Cl_2 to trigger the S(VI)/S(IV) redox reaction (Fig. 3e). These results supported a SO_2Cl_2/SO_2 positive electrode chemistry triggered by Cl_2 based on Le Chatelier's principle. The activation energies for the two pathways were acquired based on the Arrhenius equation, by measuring the electrochemical impedance spectra of the batteries at different temperatures (Supplementary Fig. 6a–c, Supplementary Table 2, and see "Methods" for details). A significantly lower activation energy of 9.3 kJ/mol was obtained by the electrolyte derived from the S(VI)/S(IV) pathway, compared to 17.5 kJ/mol for that of the S(VI)/S(III) pathway. Density functional theory calculations further revealed a reduced energy barrier of 0.84 eV for the dissociation of the S-Cl bond in SO_2Cl_2 facilitated by Cl_2, indicating the formation of thermodynamically favorable intermediates of SO_2Cl^+ and Cl_3^- can facilitate S(VI)/S(IV) reduction (Fig. 3g and Supplementary Data 1). The existence of SO_2Cl^+ intermediates during discharge was further confirmed by gas chromatography–high-resolution mass spectrometry (GC-HRMS) (Supplementary Fig. 7a-b). In contrast, the formation of $Li_2S_2O_4$ and LiCl directly from SO_2Cl_2 results in sluggish reaction kinetics in the S(VI)/S(III) redox pathway (Fig. 3h), leading to lower energy storage efficiencies and inferior rate performance.

The fast reaction kinetics of the synergistic S-Cl chemistry contribute to the high rate capability of the rechargeable Li||SO_2Cl_2-Cl_2 battery. For example, the battery could deliver a maximum current density of 400 mA/cm^2 at ~2.1 V during discharge (Fig. 4a), corresponding to a power density of 810 mW/cm^2, which is competitive compared to some recent relevant reports, including Li||S[32–35], Li||O_2[3,11,36], Li||I_2[37,38], and Li||Cl_2[39–41] batteries (Fig. 4b and Supplementary Table 1). To further promote energy storage efficiency at high current density, it is helpful to develop high-performance electrocatalysts and carbon materials to improve the positive electrode reaction kinetics. Compared with rechargeable Li(Na)||Cl_2 batteries with SO_2Cl_2 formation as an overcharged product, which demonstrated inferior reversibility[41], our Li||SO_2Cl_2-Cl_2 battery based on a synergistic S^{6+}/S^{4+} and Cl^0/Cl^- redox chemistry exhibited higher electrochemical reversibility with a higher discharge voltage, a higher energy storage efficiency, and faster reaction kinetics. The synergistic S-Cl positive electrode chemistry differs from conventional mechanisms that involve a single redox element, such as the LiCl/Cl_2 (Cl^-/Cl^0) mechanism in conventional rechargeable Li||Cl_2 batteries[41], the S/Li_2S (S^0/S^{2-}) mechanism in rechargeable Li||S batteries[42], and the irreversible SO_2Cl_2/SO_2 (S^{6+}/S^{4+}) reduction mechanism in primary Li||SO_2Cl_2 batteries[16]. The resulting fast kinetics thus affords high energy storage efficiencies of up to 99.5%, as well as a maximum current density of 400 mA/cm^2 for the obtained batteries, opening a new avenue for developing efficient and high-rate conversion-type battery systems.

Based on an optimized three-electrode cell at 10 mA/g (Supplementary Fig. 8a), the overpotentials of the positive electrode and negative electrode reactions reached 2.5 and 7.5 mV, respectively, confirming the fast reaction kinetics of the positive electrode reaction. We further confirmed this at higher specific currents from 100 to 400 mA/g (Supplementary Fig. 8a–c). We thus analyzed the solid-electrolyte interphase (SEI) layer on the Li metal negative electrode, and observed a LiCl-rich passivation layer which could suppress the parasitic reactions between the LAS electrolyte and Li metal (Supplementary Fig. 9a–d). Dense lithium deposition was observed at high current densities, *e.g.*, 400 mA/cm^2, without dendritic Li growth in our Li||SO_2Cl_2-Cl_2 batteries (Supplementary Fig. 9e–j). Long-term cycling resulted in dense lithium deposition after 50 and 100 cycles (Supplementary Fig. 9k–l). Optimizing the SEI layer can further reduce the negative electrode overpotential to enhance both energy storage efficiency and rate performance.

https://doi.org/10.1038/s41467-026-69748-8

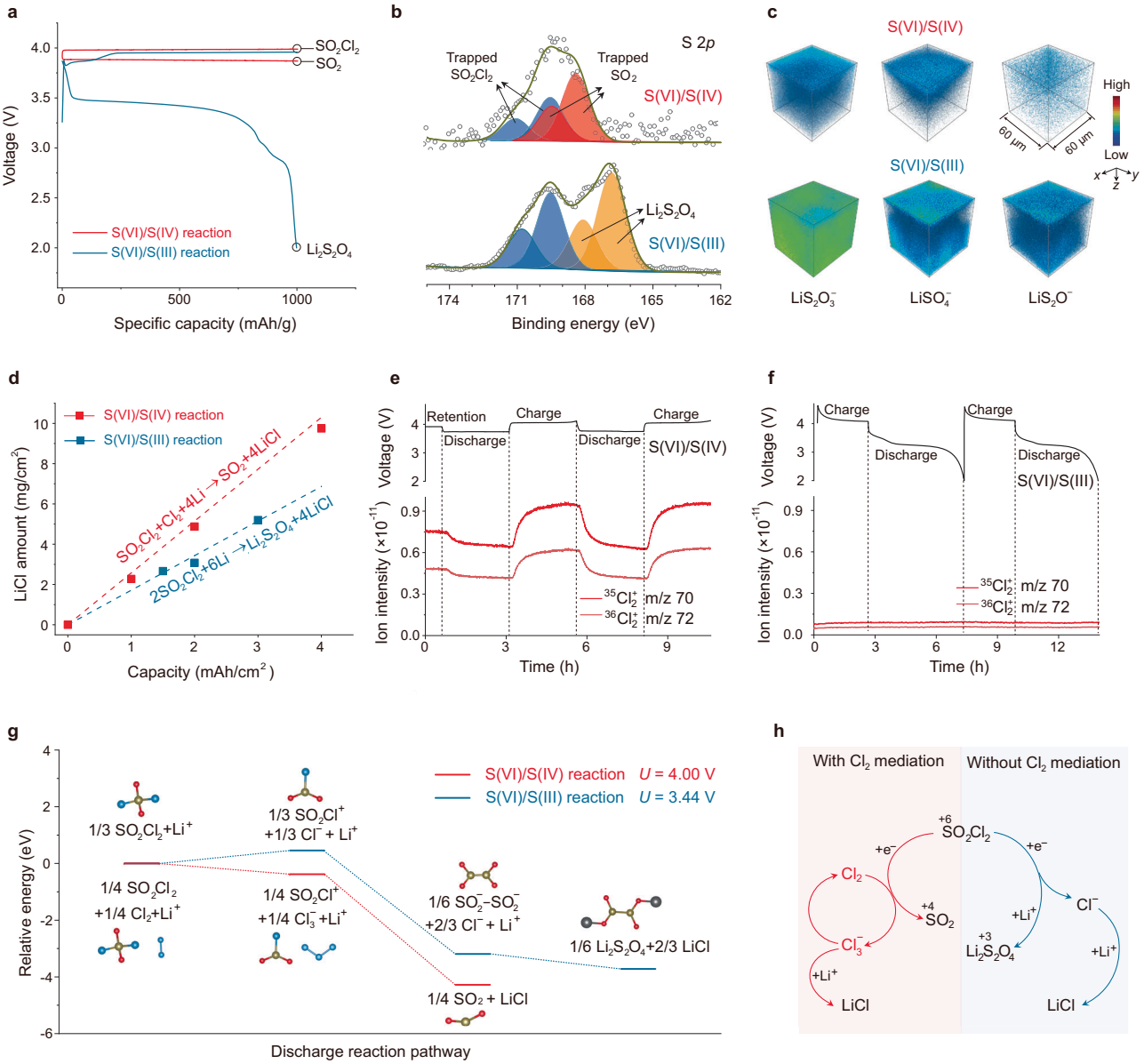

Fig. 3 | Positive electrode reactions based on S(VI)/S(IV) and S(VI)/S(III) redox chemistries. a Representative galvanostatic charge–discharge curves of the batteries based on S(VI)/S(IV) and S(VI)/S(III) redox reactions. **b** XPS S 2*p* spectra of the discharged positive electrodes from batteries based on S(VI)/S(IV) and S(VI)/S(III) redox reactions. **c** Three-dimensional distribution of discharged products on positive electrodes measured by depth profiling of TOF-SIMS. The analyzed area is 60 × 60 μm^2. The specific capacity and current are 3000 mAh/g and 400 mA/g, respectively. **d** Quantitative analysis of LiCl formation on positive electrodes at various capacities, analyzed using XRF. All positive electrodes in (**b** to **d**) were cycled for 10 cycles prior to characterization. **e**, **f** Variations of $^{35}Cl_2^+$ and $^{36}Cl_2^+$ ion intensities based on S(VI)/S(IV) and S(VI)/S(III) redox reactions acquired by in situ DEMS. The specific charge–discharge capacity in (**e**) was 500 mAh/g. The battery in (**f**) was initially discharged to 2 V, and then charged at a specific charge capacity of 500 mAh/g followed by a voltage-control protocol with a discharge cut-off voltage of 2 V. **g**, **h** Gibbs free energy calculations and schematic illustration of the S(VI)/S(IV) and S(VI)/S(III) reduction reactions, respectively. The mediation of Cl_2 is shown to reduce the dissociation energy barrier of the S-Cl bond in SO_2Cl_2 by 0.84 eV, facilitating S(VI)/S(IV) reduction via the formation of thermally favorable intermediates, such as SO_2Cl^+ and Cl_3^-. Source data for Fig. 3 are provided as a Source Data file.

We demonstrated the potential applications of our rechargeable Li||SO_2Cl_2-Cl_2 batteries in miniature and grid energy storage. A microbattery with a diameter of 3 mm was fabricated as an on-chip power supply (see "Methods"), which could reliably power a chip circuit for real-time monitoring of temperature and pressure, and transmit the collected signals to a custom-designed mobile phone *via* a wireless module, indicating the potential applications in miniature and wearable devices[43] (Supplementary Fig. 10). Notably, the Li||SO_2Cl_2-Cl_2 microbattery exhibited a maximum areal power density of 11.3 mW/mm^2, surpassing the Li||$LiFePO_4$ and Li||NCM811 counterparts by 10 times and 17 times, respectively (Fig. 4e). Moreover, the nonflammable nature of the LAS electrolyte could benefit the operation safety of the Li||SO_2Cl_2-Cl_2 batteries, as confirmed in the nail penetration test (Supplementary Fig. 11a, b).

The high energy storage efficiencies of these Li||SO_2Cl_2-Cl_2 batteries can benefit the utilization of renewable electricity. The available renewable electricity is approximatively determined by the product of input energy, energy conversion efficiency, and energy storage efficiency (Supplementary Fig. 12a). As a demonstration, we fabricated an integrated energy harvesting and storage device composed of solar cells and a Li||SO_2Cl_2-Cl_2 battery (Supplementary Fig. 12b, c), suggesting its potential in efficient utilization of renewable energy.

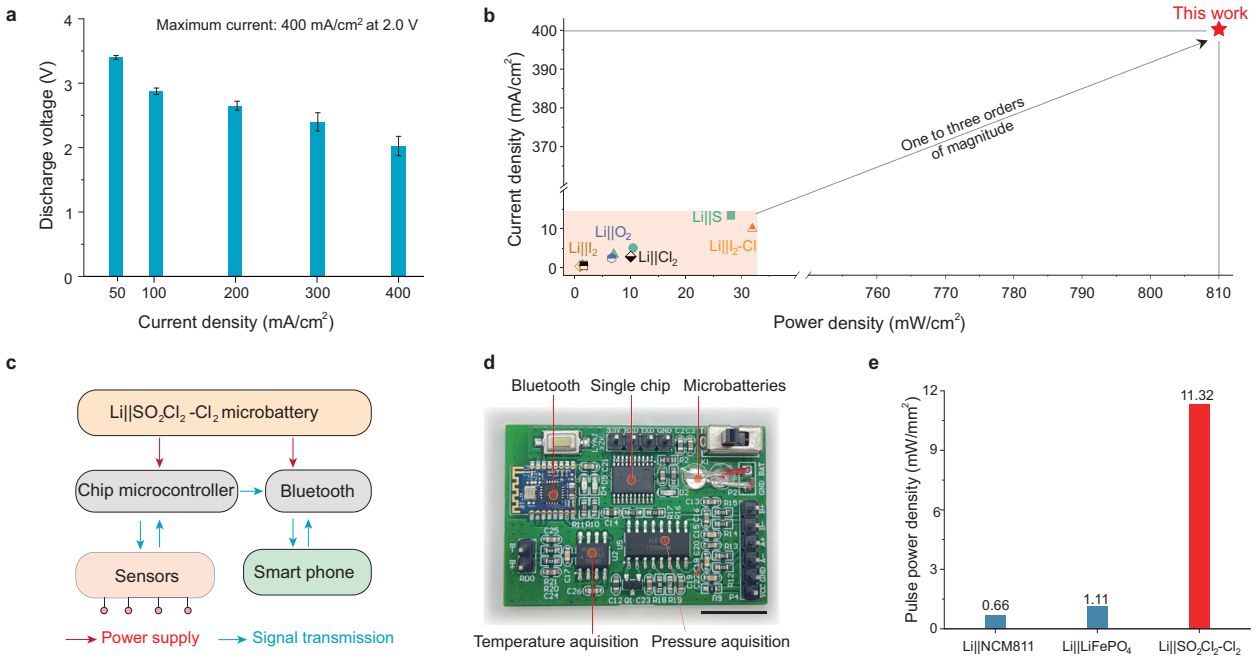

Fig. 4 | Applications and prospects of rechargeable Li||SO_2Cl_2-Cl_2 batteries. **a** Variation of discharge voltage with increasing charge–discharge current densities from 50 to 400 mA/cm² at 1 mAh/cm². Discharge voltages are presented as mean ± standard deviation. The areal capacities and current densities were based on the geometric area of the positive electrodes. The area of the positive electrode was 1.13 cm². **b** Comparison of areal current density and power density of our Li||SO_2Cl_2-Cl_2 battery and state-of-the-art Li||S[11,33–35], Li||O_2[3,36,37], Li||I_2[38,39], and Li||Cl_2[1,40,41] batteries. More details are provided in Supplementary Table 1. **c**, **d** Schematic illustration and application demonstration of a chip circuitry powered by two parallel-connected Li||SO_2Cl_2-Cl_2 microbatteries, respectively. The red and blue arrows indicate the paths of power supply and signal transmission, respectively. The detailed chip circuit diagram is provided in Supplementary Fig. 10. Scale bar, 1.0 cm. **e** Comparison of pulse power densities among Li||SO_2Cl_2-Cl_2, Li||$LiNi_{0.8}Co_{0.1}Mn_{0.1}O_2$ (NCM811), and Li||$LiFePO_4$ microbatteries. Source data for Fig. 4 are provided as a Source Data file.

Furthermore, we fabricated a fiber-shaped Li||SO_2Cl_2-Cl_2 battery with a decent energy storage efficiency of ~94% (Supplementary Fig. 12d–f and "Methods"), suggesting the promise in wearable applications. Our Li||SO_2Cl_2-Cl_2 battery also shows promise in aerospace, deep-sea, and Antarctic investigation applications. For instance, the high energy efficiency makes it promising for lunar mission, which requires efficient energy utilization to enable prolonged device operation; for deep-sea applications, the battery may offer an uninterrupted power supply for deep ocean detection and signal transmission.

We have verified the stability of the Ni current collector in LAS electrolyte by XPS analysis (Supplementary Fig. 13a). It is helpful to develop low-corrosivity additives and advanced redox mediators to reduce the electrolyte corrosivity. We also validated the applicability of different carbon materials as the positive electrode, which demonstrated decent energy efficiencies of (94.5–97.3)% (Supplementary Fig. 13b–f). For further improvement of the cycling stability, it is also promising to construct an artificial SEI layer on the negative electrode. The synergistic S-Cl positive electrode chemistry can be potentially extended to other alkali metal batteries, such as Na and K batteries, as well as multivalent metal batteries, such as Mg and Al metal batteries, towards higher elemental abundance and lower material cost. Further efforts can be made to reduce the corrosivity of electrolyte and active materials. Besides, it is helpful to address the shuttle effect of the redox products during cycling, thus promoting the electrochemical reversibility of the positive electrode chemistry.

Discussion

In conclusion, we report a rechargeable battery with energy storage efficiencies of up to 99.5%. We show that the synergistic S-Cl battery chemistry, based on a SO_2/SO_2Cl_2 redox chemistry mediated by in situ formed Cl_2, can achieve fast reaction kinetics. The understanding of the synergistic S-Cl battery chemistry is expected to facilitate the designing and screening of new electrode and electrolyte materials to improve the energy storage efficiency and rate capability of current electrochemical energy storage technologies. With potential applications in grid-scale energy storage, integrated circuits, and wearable devices, the rechargeable Li||SO_2Cl_2-Cl_2 battery opens a new avenue for high-efficiency and fast energy storage solutions.

Methods

Materials

SO_2Cl_2 (98%+, Adamas), $AlCl_3$ (98%, TCI), and LiCl (Water <10 ppm, 99.99%, Adamas), dichloroethane (99.5%, Adamas), methyl dichloroacetate (MTFA, 97%+, Adamas) and ethanol (99.5%, Adamas) were used without any purification. Ketjenblack (ECP-600JD) and polytetrafluoroethylene (PTFE) emulsion binder (60 wt% in ethanol, D210C) were purchased from Cyber Electrochemical Materials. Battery-level lithium bisfluorosulfonimide (LiFSI, >99.9%, water ≤ 100 ppm) was purchased from DoDoChem. Li metal chips (15 mm diameter, 200 μm thickness, >99.9%), Li metal belts (250 μm thickness, >99.9%), and ceramic-coated polypropylene separator (PP) were purchased from Canrd New Energy Technology Co., Ltd. The Li metal was stored at 25 °C in the argon-filled glovebox with water and oxygen contents below 1 ppm before use. Reduced graphene oxide, multi-walled carbon nanotube were purchased from Nanjing XFNANO Materials Tech Co., Ltd. The nickel (Ni) foam (0.5 mm in thickness, 99.8%) was purchased from Cyber Electrochemical Materials. The Ni foams with a diameter of 14 mm were fabricated using a manual disk cutter (MTI, MSK-T-10), followed by cleaning in ethanol under

ultrasonication for 15 min. LiCl and LiFSI were dried under vacuum for 24 h at 100 °C before use.

Preparation of the electrolytes and electrodes

All the electrolytes were prepared in an argon-filled glovebox with water and oxygen contents below 1 ppm. For LAS electrolyte preparation, 3.6 M LiCl and 3.6 M $AlCl_3$ were added to SO_2Cl_2 in a 20-mL glass vial and stirred for 1 h to produce a transparent, light-yellow electrolyte at 25 °C, which was immediately used for battery assembly. For the positive electrode preparation, Ketjenblack and PTFE emulsion (binder) were mixed in ethanol at a mass ratio of 9:1, followed by ultrasonic treatment to form a uniform slurry at 25 °C. For coin cell production, 150 µL of the above slurry was dipped onto a Ni foam (0.5 mm in thickness, 12 or 14 mm in diameter) using a pipette (150 µL was added each time by dropwise addition), until the areal loading of ketjenblack reached 1–2 mg/cm^2 (double-side coated), followed by drying at 120 °C for 2 h. For rate performance tests in Fig. 4a, b, the mass loading of Ketjenblack was 8–10 mg/cm^2 on a piece of Ni foam with a diameter of 12 mm. Circular Li metal foils with a diameter of 16 mm were used as the negative electrode for coin cells.

Battery preparation and electrochemical measurements

All the cells were assembled in the argon-filled glovebox with water and oxygen contents below 1 ppm. The glass fiber separators were dried under vacuum for 24 h at 110 °C before use. Coin cells (2032 type, grade 316 stainless steel) were assembled using a Li metal foil as the negative electrode, a Ketjenblack positive electrode, and a glass fiber separator (16 mm, GF/D, thickness of 675 µm, Whatman) with 180 µL LAS electrolyte. For preparing coin cells with high areal capacities of 7.8–13 mAh/cm^2, ~1 mL LAS electrolyte was used. For all cells, an excess of lithium metal was employed at the negative electrode. For pouch cells, a Li foil negative electrode (4 × 4 cm^2) and a Ketjenblack positive electrode (4×4 cm^2) were pasted on both sides of an aluminum laminated pouch using carbon tape, with the use of Ni tabs as the current collectors. Two glass fiber separators (GF/A, Whatman, 4.3 × 4.3 cm^2) were used with approximately 6 − 10 mL electrolyte. The Ketjenblack mass loadings were 6 − 10 mg/cm^2 for pouch cells. The pouch cells were tested under a pressure of ~1.0 MPa. Electrochemical measurements were conducted using a Neware battery testing system (CT-4008-5V50mA or CT-4008-5V6A). The cells were tested at 25 °C in a thermostatic test chamber (Neware MHW-200). The low-temperature electrochemical characterizations were performed using a 0 °C freezer (Frestech Group) and a − 20 °C freezer (Hicon Industry Co.,Ltd). Electrochemical impedance spectroscopy was performed with a CHI660E electrochemical workstation. At least three independent cells were tested for each electrochemical experiment, including but not limited to galvanostatic cycling and rate capability measurements. Prior to the EIS measurements, the cell was retained at the open-circuit voltage (OCV) condition for 10 min for stabilization and was conducted under potentiostatic conditions. The frequency range was 10^{-1} to 10^6 Hz at an amplitude of 5 mV, and 12 data points were collected per decade of frequency.

A capacity-limited protocol was applied for the S(VI)/S(IV) pathway[44], while a voltage-limited protocol with a cut-off voltage of 2.0 V during discharge was applied for the S(VI)/S(III) pathway. The specific capacities and specific currents were calculated based on the mass of Ketjenblack on the positive electrode unless otherwise specified. For the fabrication of Li||SO_2Cl_2-Cl_2 microbattery, a 3 mm-diameter lithium metal negative electrode, and a 3 mm-diameter Ketjenblack/aluminum foil positive electrode (loading: 4 mg/cm^2), were separated by a single piece of LAS electrolyte-soaked GFD separator (3 mm in diameter). The assembled Li||SO_2Cl_2-Cl_2 microbattery was mechanically compressed and edge-sealed with epoxy and organic silicone gel for the on-chip power supply demonstration. For the fabrication of rechargeable Li||SO_2Cl_2-Cl_2 fiber batteries, a multi-walled carbon nanotube fiber (diameter of ~20 µm) was deposited with Li metal at ~250 mAh/g and 100 mA/g serving as the negative electrode. Another multi-walled carbon nanotube fiber was used as the positive electrode. These fiber electrodes were separated by a polypropylene separator infiltrated with a gel electrolyte comprised of 3.6 M $AlCl_3$ and 2 M LiFSI in SO_2Cl_2. The fiber battery was encapsulated in a PTFE tube (inner diameter 2.5 mm, outer diameter 3 mm) using epoxy and organic silicone gel.

Calculation of energy storage efficiency

The energy storage efficiency ($E_{storage}$) is calculated based on the following equation:

$$E_{storage} = \frac{U_{discharge} \times C_{discharge}}{U_{charge} \times C_{charge}}$$

where $U_{discharge}$ and U_{charge} are the average discharge and charge voltages, respectively; $C_{discharge}$ and C_{charge} are the discharge and charge capacities, respectively.

Calculation of power density

The power density (P) of batteries can be calculated as follows:

$$P = \frac{U_{avg} \times I}{S}$$

where U_{avg} represents the discharge voltage (V); I represents the discharge current (mA); S represents the area (cm^2) of positive electrode.

Characterizations

X-ray diffraction was conducted using a Bruker D8 Advance power X-ray diffractometer with Cu Kα radiation (λ = 1.54056 Å) at 40 kV and 40 mA. The crystalline structures were indexed to the Joint Committee on Powder Diffraction Standards (JCPDS) cards. Prior to ex situ XRD characterization, all samples were hermetically sealed in an airtight sample holder in an Ar-filled glovebox. Scanning electron microscopy was conducted on a ZEISS GeminiSEM 300. Cryogenic transmission electron microscopy was performed with a Talos F200X G2 microscope under liquid nitrogen at an accelerating voltage of 200 kV. The electrode powders were scraped from the current collectors, which were ultrasonically dispersed in dichloroethane and dipped on a carbon film-covered copper microgrid in an argon atmosphere. The grid was then transferred to a cryo-holder (Fischione 2550) in an argon-filled glovebox and quickly inserted into the microscope with a liquid nitrogen environment. The ionic conductivities of the electrolytes were measured using a FE38 ionic conductor (FiveEasy Plus), with calibration at various temperatures. Time-of-flight secondary ion mass spectroscopy was conducted with an ION-TOF5-100 instrument under a chamber pressure of 1.1 × 10^{-9} mbar. The secondary ions from the sample surface were sputtered by a Bi^{3+} ion beam, with a Cs^+ secondary gun operating at 2 keV over a 60 µm×60 µm area. Depth profiling was achieved by sputtering the electrode surfaces for the same duration. X-ray photoelectron spectroscopy was conducted using a 250XI + X-ray photoelectron spectrometer (Thermo Fisher Scientific) with a monochromatic Al Kα radiation source ($h\nu$ = 1486.6 eV) and a charge neutralization system, under a vacuum below 5 × 10^{-9} Torr. All the samples were transferred to an air-isolated chamber. The binding energies were calibrated with the C 1 s peak at 284.8 eV. Differential electrochemical mass spectrometry was carried out using a commercial quadrupole mass spectrometer (Linglu Instrument) and a custom-designed Swagelok battery equipped with two poly(ether-ether-ketone) capillary tubes for gas inlet and outlet. The battery comprised a Ketjenblack positive electrode (diameter of 19 mm, 4 mg/cm^2), a Li foil (diameter of 19 mm), and a GF/D separator (diameter of 20 mm) with 400 µL electrolyte. The cell was first flushed with argon gas for 4-6 h to calibrate the baseline, followed by being charged and discharged at 400 mA/g

for gas analysis. To avoid the ion intensity decay caused by SO_2Cl_2 volatilization, the ion intensities were normalized against baseline signals during testing. X-ray absorption spectroscopy (XAS) was conducted at the 4B7A station of Beijing Synchrotron Radiation Facility (BSRF, operated at 2.5 GeV with a maximum current of 250 mA), using a Si (111) double-crystal monochromator. The spectra were collected in a fluorescence model with a silicon drift detector. XAS standard samples were measured in a total electron yield mode under vacuum (10^{-3} to 10^{-4} Pa). All the XAS spectra were aligned, normalized, and merged using Athena software. Raman spectra of the electrolytes were recorded using a Horiba LabRAM Solei Raman spectrometer with a 532 nm HeNe laser excitation source. Before the ex situ Raman tests, all electrolyte samples were placed in capillaries with both ends sealed using organic adhesive in an Ar-filled glovebox. X-ray fluorescence (XRF) analysis of positive electrodes was performed on an energy dispersive XRF spectrometer (Shimadzu). The LiCl quantification was determined by analyzing the characteristic X-ray signal of Cl^- from the positive electrode. Prior to the XRF measurements, the positive electrodes were rinsed with SO_2Cl_2 to remove the salts in the electrolyte, followed by vacuum drying overnight to remove SO_2Cl_2. To avoid Cl_2 interference possibly trapped in the carbon pores after the vacuum treatment[45], we applied a baseline correction using extrapolation to a zero-capacity condition, assuming that the amount of Cl^- is zero when the capacity is zero. For calibration, external standards were prepared using NaCl-loaded Ketjenblack/Ni foam samples with various mass loadings. Gas chromatography–high-resolution mass spectrometry (GC-HRMS) was performed on a gas chromatography–quadrupole/Orbitrap mass spectrometry system (Orbitrap Exploris GC240, Thermo Scientific, USA). Specifically, Coin cells were potentiostatically held at 0%, 25%, 50%, and 100% of state-of-charge (5th cycle, 2000 mAh/g and 400 mA/g), and quickly disassembled in an argon-filled glovebox. SO_2Cl^+ species were extracted from the positive electrodes via immersion in 1,2-dichloroethane (DCE) for 1 h after being fully rinsed and dried. The extracted species were tested under positive mode on GC-HRMS using electron impact (EI). The three-electrode cell uses a Swagelok-type configuration, where the Ag/AgCl electrode was separated from the LAS electrolyte with porous ceramics and filled with a 1.0 M $LiAlCl_4$-SO_2Cl_2 solution for balancing Cl^- concentrations and maintaining a constant electrochemical interface.

Calculations of the activation energy

The activation energies for the electrolytes from S(VI)/S(IV) and S(VI)/S(III) pathways were determined by electrochemical impedance spectroscopy using Li-Li symmetric cells at various temperatures of 303.15, 313.15, 323.15, and 333.15 K. For the S(VI)/S(III) pathway, the electrolyte was prepared by applying a voltage-limited protocol in a tightly sealed glass reactor containing 5 mL of LAS electrolyte. For the S(VI)/S(IV) pathway, the electrolyte was prepared using a capacity-limited protocol with a specific charge/discharge capacity of 500 mAh/g. The Li-Li symmetric cells were fabricated using the above two electrolytes and cycled for 100 cycles at 0.52 mA/cm^2 and 0.52 mAh/cm^2. The activation energies were calculated using the Arrhenius equation:

$$\frac{1}{R_{ct}} = A_0 e^{-E_a/RT}$$

Where R_{ct} is the charge transfer resistance calculated based on the Nyquist plots, A_0 is the pre-exponential factor, T is the Kelvin temperature, R is the standard gas constant of 8.314 J/(mol·K). E_a is the activation energy, which was derived using the slope of $\ln(1/R_{ct})$ with the reciprocal temperature of $1000/T$ in plots:

$$E_a = -8.314 \times \text{slope}(\text{kJ/mol})$$

Density functional theory calculations

All the calculations were carried out using density functional theory as implemented in the VASP code[46]. Electronic exchange–correlation energy was modeled using the Perdew–Burke–Ernzerhof function within a generalized gradient approximation[47]. The projector-augmented wave method was used to describe the ionic cores[48,49]. For the plane-wave expansion, a 450 eV kinetic energy cut-off was used following testing a series of different cut-off energies. The convergence criterion for the electronic structure iteration was set to 10^{-4} eV, and that for geometry optimization was 0.01 eV/Å on force.

The Gibbs free energy was calculated based on the density functional theory-based energy (E), zero-point energy (ZPE), and the entropy (TS) by using the following expression:

$$G = E + ZPE - TS$$

The change in the Gibbs free energy (ΔG) can be calculated by using the electron-transfer numbers (n) and the difference in the electrochemical potential (ΔU).

$$\Delta G = -ne\Delta U$$

The difference in ΔG between the positive electrode and negative electrode is the cell operation voltage with single-electron transfer ($n = 1$).

Data availability

The data that support the plots within this paper and other findings of this study are available from the corresponding author upon reasonable request. Source data are provided with this paper.

References

1. Tarascon, J. M. & Armand, M. Issues and challenges facing rechargeable lithium batteries. *Nature* **414**, 359–367 (2001).
2. Choi, J. & Aurbach, D. Promise and reality of post-lithium-ion batteries with high energy densities. *Nat. Rev. Mater.* **1**, 16013 (2016).
3. Alireza, K. et al. A room temperature rechargeable Li_2O-based lithium-air battery enabled by a solid electrolyte. *Science* **379**, 499 (2023).
4. Cheng, C. et al. Pumped hydro energy storage and 100 % renewable electricity for East Asia. *Global Energy Interconnection* **2**, 386–392 (2019).
5. Energy Institute Statistical Review of World Energy 2024. https://www.energyinst.org/statistical-review (2024).
6. Bruce, D. et al. Electrical energy storage for the grid: a battery of choices. *Science* **334**, 928–935 (2011).
7. Sutherland, B. R. Charging up stationary energy storage. *Joule* **3**, 1–3 (2019).
8. Yu, S. H. et al. Understanding conversion–type electrodes for lithium rechargeable batteries. *Acc. Chem. Res.* **51**, 273–281 (2018).
9. Sun, Y., Liu, N. & Cui, Y. Promises and challenges of nanomaterials for lithium-based rechargeable batteries. *Nat. Energy* **1**, 71 (2016).
10. Zhou, J. et al. Healable and conductive sulfur iodide for solid-state Li–S batteries. *Nature* **627**, 301–305 (2024).
11. Qiao, Y. et al. A high-energy-density and long-life lithium-ion battery via reversible oxide–peroxide conversion. *Nat. Catal.* **2**, 1035–1044 (2019).
12. Ye, L. et al. A rechargeable calcium–oxygen battery that operates at room temperature. *Nature* **626**, 313–318 (2024).
13. Lv, Y. et al. Implantable and bio-compatible Na-O_2 battery. *Chem* **10**, 1885–1896 (2024).
14. Ahn, S. et al. Why charging Li–air batteries with current low-voltage mediators is slow and singlet oxygen does not explain degradation. *Nat. Chem.* **15**, 1022–1029 (2023).
15. Zhao, M. et al. Kinetic promoters for sulfur cathodes in lithium–sulfur batteries. *Acc. Chem. Res.* **57**, 547–557 (2024).

16. Gilman, S. et al. The reduction of sulfuryl chloride at Teflon-bonded carbon cathodes. *J. Electrochem. Soc.* **127**, 1427–1432 (1980).
17. Abraham, K. M. et al. Chemical and electrochemical processes in some lithium-liquid cathode batteries. *J. Power Sources* **34**, 81–101 (1991).
18. Murphy, R. M. et al. The technology of the Li/Cl_2 in SO_2Cl_2 cell system IV. high temperature performance, storability, and safety characteristics. *J. Appl. Electrochem.* **13**, 439–449 (1983).
19. Liang, C. C. et al. The Li/Cl_2 in SO_2Cl_2 inorganic battery system. *J. Electrochem. Soc.* **128**, 1631–1636 (1981).
20. Hitchcock, A. P. et al. Sulfur and chlorine K-shell X-ray absorption spectra of SCl_2, S_2Cl_2, $SOCl_2$ and SO_2Cl_2. *Chem. Phys.* **115**, 93–101 (1987).
21. Yang, C. et al. Aqueous Li-ion battery enabled by halogen conversion-intercalation chemistry in graphite. *Nature* **569**, 245–250 (2019).
22. Thomas, R. W., Wade, J. & Wood, B. J. The bonding environment of chlorine in silicate melts. *Chem. Geol.* **617**, 121269 (2023).
23. Sun, W. et al. A rechargeable zinc-air battery based on zinc peroxide chemistry. *Science* **371**, 46–51 (2021).
24. Guan, Z. et al. Low concentration electrolyte enabling anti–clustering of lithium polysulfides and 3D–growth of Li_2S for low temperature Li–S conversion chemistry. *Adv. Energy Mater.* **13**, 2302850 (2023).
25. Gao, N. et al. Low-temperature Li–S battery enabled by CoFe bimetallic catalysts. *J. Mater. Chem. A* **10**, 8378–8389 (2022).
26. Xu, J. et al. Realizing all–climate Li–S batteries by using a porous sub–nano aromatic framework. *Angew. Chem. Int. Ed.* **61**, e202211933 (2022).
27. Liang, P. et al. Rechargeable Li/Cl_2 battery down to −80°C. *Adv. Mater.* **36**, 2307192 (2024).
28. Yuan, B. et al. Unlocking reversible silicon redox for high–performing chlorine batteries. *Angew. Chem. Int. Ed.* **62**, e202306789 (2023).
29. Lim, H. D. et al. A new perspective on Li–SO_2 batteries for rechargeable systems. *Angew. Chem. Int. Ed.* **54**, 9663–9667 (2015).
30. Grundish, N., Amos, C. & Goodenough, J. B. Communication–characterization of $LiAlCl_4{\cdot}xSO_2$ inorganic liquid Li^+ electrolyte. *J. Electrochem. Soc.* **165**, A1694–A1696 (2018).
31. Li, H. et al. Developing high-power Li||S batteries via transition metal/carbon nanocomposite electrocatalyst engineering. *Nat. Nanotechnol.* **19**, 792–799 (2024).
32. Zhou, S. et al. Visualizing interfacial collective reaction behavior of Li–S batteries. *Nature* **621**, 75–81 (2023).
33. Wu, X. et al. Redox mediator: A new strategy in designing cathode for prompting redox process of Li-S batteries. *Adv. Sci.* **6**, 1900958 (2019).
34. Han, Z. et al. Machine-learning-assisted design of a binary descriptor to decipher electronic and structural effects on sulfur reduction kinetics. *Nat. Catal.* **6**, 1073–1086 (2023).
35. Wu, M. et al. Highly reversible diphenyl trisulfide catholyte for rechargeable lithium batteries. *ACS Energy Lett.* **1**, 1221–1226 (2016).
36. Wu, S. et al. Clean electrocatalysis in a Li_2O_2 redox-based Li–O_2 battery built with a hydrate-melt electrolyte. *ACS Catal.* **8**, 1082–1089 (2018).
37. Nikiforidis, G., Tajima, K. & Byon, H. R. High energy efficiency and stability for photoassisted aqueous lithium–iodine redox batteries. *ACS Energy Lett.* **1**, 806–813 (2016).
38. Cheng, Z. et al. Achieving long cycle life for all-solid-state rechargeable Li-I_2 battery by a confined dissolution strategy. *Nat. Commun.* **13**, 125 (2022).
39. Zhu, G. et al. High-capacity rechargeable Li/Cl_2 batteries with graphite positive electrodes. *J. Am. Chem. Soc.* **144**, 22505–22513 (2022).
40. Chen, G. et al. Transforming a primary Li-$SOCl_2$ battery into a high-power rechargeable system via molecular catalysis. *J. Am. Chem. Soc.* **145**, 22158–22167 (2023).
41. Zhu, G. et al. Rechargeable Na/Cl_2 and Li/Cl_2 batteries. *Nature* **596**, 525–530 (2021).
42. Manthiram, A. et al. Rechargeable lithium–sulfur batteries. *Chem. Rev.* **114**, 11751–11787 (2014).
43. Longchamps, R. S. et al. Battery electronification: intracell actuation and thermal management. *Nat. Commun.* **15**, 5373 (2024).
44. Lu, J. et al. A lithium-oxygen battery based on lithium superoxide. *Nature* **529**, 377–382 (2016).
45. Zhu, G. et al. Shedding light on rechargeable Na/Cl_2 battery. *Proc. Natl. Acad. Sci. USA.* **120**, e2310903120 (2023).
46. Kresse, G. & Furthmüller, J. Efficiency of ab-initio total energy calculations for metals and semiconductors using a plane-wave basis set. *Comp. Mater. Sci.* **6**, 15–51 (1996).
47. Perdew, J., Burke, K. & Ernzerhof, M. Generalized gradient approximation made simple. *Phys. Rev. Lett* **77**, 18–28 (1996).
48. Blöchl, P. E. Projector augmented-wave method. *Phys. Rev. B* **50**, 17953–17979 (1994).
49. Kresse, G. & Joubert, D. From ultrasoft pseudopotentials to the projector augmented-wave method. *Phys. Rev. B* **59**, 1758 (1999).

Acknowledgements

This work was supported by the National Natural Science Foundation of China (22575145 and 22209108), the Scientific Research Innovation Capability Support Project for Young Faculty (SRICSPYF-ZY2025049), the Fundamental Research Funds for the Central Universities (23×010301599), and the Autonomous Project of State Key Laboratory of Synergistic Chem-Bio Synthesis (sklscbs202557). The authors acknowledge the 4B7A station at the Beijing Synchrotron Radiation Facility.

Author contributions

H.S. and H.P. conceived and designed the research project. X.Z. and S.G. prepared electrodes and electrolytes, fabricated batteries, and conducted electrochemical measurements. M.L., L.Y., Z.O. and X.Z. prepared fiber batteries and on-chip microbatteries. S.G., Q.X., B.Y., Y.W. and S.T. performed Raman spectroscopy, time-of-flight secondary ion mass spectrometry, X-ray absorption spectroscopy, and X-ray fluorescence. Q.X., S.G., and X.Z. performed differential electrochemical mass spectrometry and gas chromatography–high-resolution mass spectrometry. Z.O., X.Z., C.Z., and S.W. performed scanning electron microscopy and transmission electron microscopy. L.W. performed the simulation calculations. X.Z., M.L., S.G., H.P., and H.S. prepared the manuscript. All the authors participated in data analysis and discussion.

Competing interests

The authors declare no competing interests.

Additional information

Supplementary information The online version contains supplementary material available at https://doi.org/10.1038/s41467-026-69748-8.

Correspondence and requests for materials should be addressed to Huisheng Peng or Hao Sun.

Peer review information *Nature Communications* thanks Linjie Zhi and the other anonymous reviewer(s) for their contribution to the peer review of this work. [A peer review file is available].